Solid State Phenomena
ISSN: 1662-9779, Vol. 388, pp 101-111
doi:10.4028/p-Vg6Uo9

Submitted: 2026-01-19
Revised: 2026-02-20
Accepted: 2026-02-20
Online: 2026-04-15

A Comparative Study of Multiple Cutting Methods on Thin Ferritic Steel for Tensile Test Experiment

Tarek Azzouni[1,a,*], Lysimachi Iona[1,b], Patrick Hegele[2,c], Wolfram Volk[1,d], and Christoph Hartmann[1,e]

[1]Chair of Metal Forming and Casting, Technical University of Munich, Walther-Meißner-Straße 4, 85748 Garching, Germany

[2]Institute of Materials Science, Technical University of Munich, Boltzmannstr. 15, 85748 Garching bei München, Germany

[a] tarek.azzouni@tum.de, [b] lysimatchi.iona@tum.de, [c] patrick.hagele@tum.de, [d] wolfram.volk@utg.de, [e] christoph.hartmann@utg.de

Keywords: Residual Stress, Tensile Test, Thin Metal Sheet.

Abstract.This study investigates the effects of various cutting technologies on a 0.25 mm thick ferritic steel, a material widely used in packaging and other lightweight applications. The study provides a comprehensive comparison of four distinct cutting technologies: Laser Cutting, Milling, Electrical Discharge Machining (EDM), and Water Jet Cutting. The research focuses on the impact of these cutting processes on the material's properties and its performance under uniaxial tension. X-ray diffraction is used to precisely measure the magnitude and distribution of residual stresses along the cut edge in order to correlate them with changes in the material's flow curve, which is critical for accurate mechanical characterization. Furthermore, a laser-scanning microscope was used for detailed morphological analysis of the cut edge and for roughness measurement. To quantify mechanical property changes, microindentation hardness testing was used to assess the degree of work hardening induced by each cutting method. Finally, Digital Imaging Correlation (DIC) was employed to track strain distribution and observe strain field variations.

Introduction

Ferritic steels have increasingly become the material of choice for the automotive, construction, and household appliance sectors, primarily due to their superior resistance to stress corrosion cracking [1] and cost efficiency compared to their austenitic counterparts. While this cost advantage is largely attributed to low or negligible nickel content, the adoption of thin ferritic steel for these applications creates specific metallurgical challenges. In particular, $0.25mm$-thick sheets are crucial for applications requiring lightweight yet durable components, such as exhaust systems and catalytic converter shells. However, processing these thin sheets presents specific manufacturing challenges that differ significantly from those of widely used thicker sheet metals [2].

The transition to thin-sheet processing disproportionately amplifies the impact of cutting methodology on component quality. Unlike thicker plates, where the bulk material acts as a heat sink, thin ferritic sheets (often less than 2mm thick) lack the thermal capacity to dissipate energy effectively. Consequently, thermal cutting methods can lead to rapid heat accumulation at the cut edge [3]. Without precise control, this localized heat input can induce a larger Heat-Affected Zone (HAZ), potentially rendering the edge brittle and susceptible to microcracking [4].

With rapid advancements in cutting technologies [5], the surface properties resulting from these machining operations have gained critical importance. Machining quality is no longer defined by dimensional accuracy, but is characterized by microstructural alterations, edge deformation, surface roughness, and kerf geometry. Consequently, the primary objective is to identify a methodology that balances processing speed and cost-efficiency with minimal edge deformation.

This paper examines the cutting characteristics of thin ferritic steel, focusing on edge integrity, by analyzing multiple cutting approaches and their effects on microstructural and geometric features. The

novelty of this work lies in its systematic comparison of multiple industrial cutting methods applied to thin ferritic sheets under controlled conditions, with particular focus on quantifying HAZ extent and edge hardening that are only partially addressed in existing studies on thicker materials or different steel grades. To achieve this, a structured experimental programme is conducted, including a series of cutting methods followed by metallographic examination, microhardness profiling, and surface/edge geometry measurements, enabling a comprehensive assessment of how each cutting process affects edge integrity and, ultimately, component performance. Specifically distinguishing between effects on the bulk plastic flow behavior and the localization of failure.

Material Preparation:

Experimental investigations were conducted on a 0.25 mm-thick ferritic steel developed at Thyssen - Krupp Rasselstein GmBH, to evaluate the influence of cutting methodology on the material's tensile performance. The specimen geometry, illustrated in Figure 1, complies with the ISO-6892-1 standard [6]. To assess the impact of edge preparation, specimens were fabricated using four distinct methodologies: Electrical Discharge Machining (EDM) processed using a Agiecut Excellence 2F, Water Jet Machining performed on an OMAX MicroMAX system operating at $22°C$ with a precision of $\pm 2.5\mu m$; Milling conducted using a Deckel Maho FP3-50 machining center; and Laser Cutting executed using a Trumpf Trulaser 3030 (L20) CO_2 laser with a power output of 4 kW.

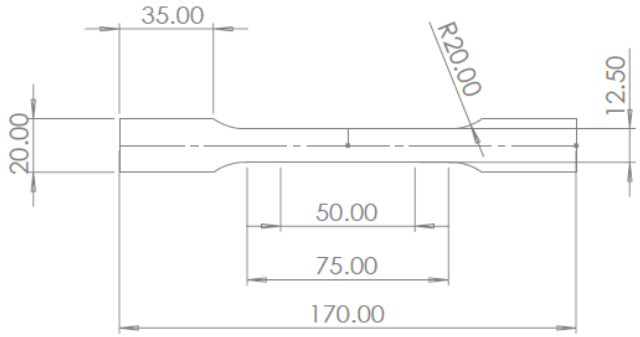

Fig. 1: Suitable Tensile Geometry according to ISO-6892-1 for Thin Metal Sheet

Characterization Methodology and Results

After sample preparation, multiple characterizations were performed to identify which mechanisms may have influenced the tensile test results.

Microscopic images and roughness calculation.

Surface morphology images for each cutting method were obtained using a VK-X150K 3D laser-scanning confocal microscope (Keyence, Japan). The laser-scanning microscope provides a detailed depiction of the cutting surface, compensating for height differences and focus issues that may arise from surface abnormalities. In addition, line roughness measurements were performed along three vertical lines and one horizontal line located at the mid-thickness of the specimen. An area surface roughness measurement was also conducted over a rectangular region bounded by vertical lines 1 and 3, as illustrated in Figure 2.

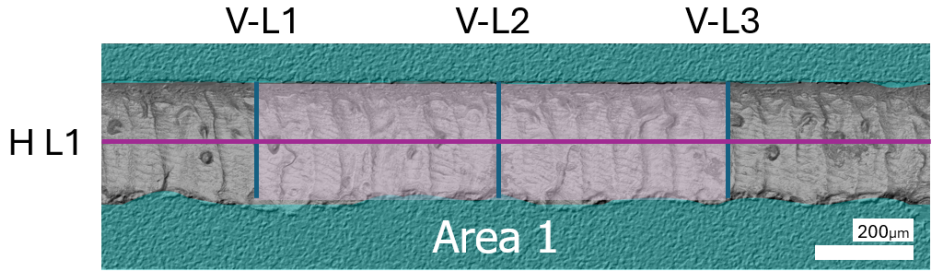

Fig. 2: Illustration of the lines and surface where measurements were performed.

The high quality of the acquired images is evident for both laser-cut and milling-cut surfaces, which clearly reveal the trajectory of the respective cutting tools (Fig. 3a & 3b). In contrast, no distinct surface pattern is observed for the EDM-cut specimens (Fig. 3c). Most notably, the water-jet-cut surface exhibits a highly irregular morphology (Fig. 3d). These qualitative observations are supported by the roughness measurements summarized in Table 1.

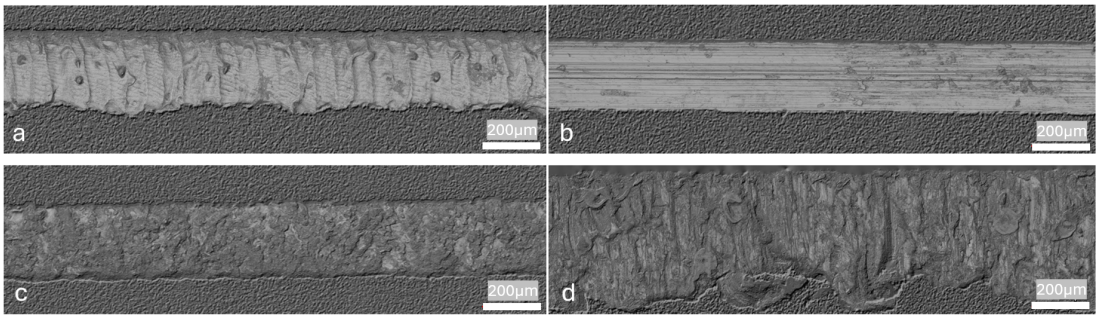

Fig. 3: Images of the cutting edge of: a) Laser Cut, b) Milling Cut, c) EDM cut, and d) Water Jet cut.

The arithmetical mean roughness (R_a) quantifies the average absolute deviation of the surface height from the mean line, as defined in Equation 1:

$$R_a = \frac{1}{n}\sum_{i=1}^{n}|Z_i| \tag{1}$$

where n represents the total number of measured points and Z_i denotes the vertical deviation (height) from the mean line at a specific point i.The roughness was evaluated along all vertical and horizontal line profiles. The highest R_a values were observed for water-jet-cut surfaces, followed by EDM. In both processes, the resulting surface finish is significantly influenced by factors such as cut velocity and wire type. Conversely, the lowest values were measured for the milled surfaces, followed by the laser-cut specimens, where the use of a pulsed laser resulted in a finer finish. This ranking was consistent across all measurement lines, except for vertical line 3. Furthermore, the areal arithmetical mean height (S_a) analysis confirmed this trend.

Table 1: Surface roughness parameters

Method	**Horiz.Line 1**	**Vertic.Line 1**	**Vertic.Line 2**	**Vertic.Line 3**	**Area 1**	
	Ra (μm)	Ra (μm)	Ra (μm)	Ra (μm)	Sa (μm)	Str
EDM Cut	12.673	7.042	9.154	3.631	11.474	0.154
Laser Cut	6.082	5.361	5.604	8.356	7.905	0.036
Milling Cut	0.736	2.445	3.746	2.909	1.890	0.024
Water Jet Cut	23.987	8.864	10.310	7.388	23.079	0.217

Residual stress measurement.

In this experiment, X-ray diffraction is used to measure the crystal lattice distance, d. which is calculated from the diffraction angle 2θ using Bragg's Law. Since macrostresses produce uniform distortion across many crystals, they shift the angular position of the diffraction peak [7]. The technique relies on measuring these elastic strains and calculating the residual stress producing them, assuming a linear elastic distortion of the crystal lattice [8].

For engineering applications, a plane-stress elastic model is used because the X-ray penetration depth is low in most cases, typically less than $5 - 6\ \mu m$ [9]. In this thin surface layer, the material is assumed to be in a state of plane stress where the principal stresses, σ_{11} and σ_{22}, act only in the plane of the surface. Consequently, there is no stress component perpendicular to the free surface ($\sigma_{33} = 0$), and the shear stresses acting out of the plane (σ_{13} and σ_{23}) are also zero. Although there is no stress perpendicular to the surface, a strain component perpendicular to the surface does exist due to Poisson's ratio contractions caused by the principal stresses [10]. For this reason, multiple tensile specimens (TS) are assembled and secured using a clamping system. This approach increases the thickness and eliminates the need to calibrate the XRD beam at the edges (due to the 1mm beam width and the 0.25mm specimen thickness, this may have posed a problem during alignment). By stacking multiple samples, the measurement area gets bigger, as illustrated in the Figure.4.

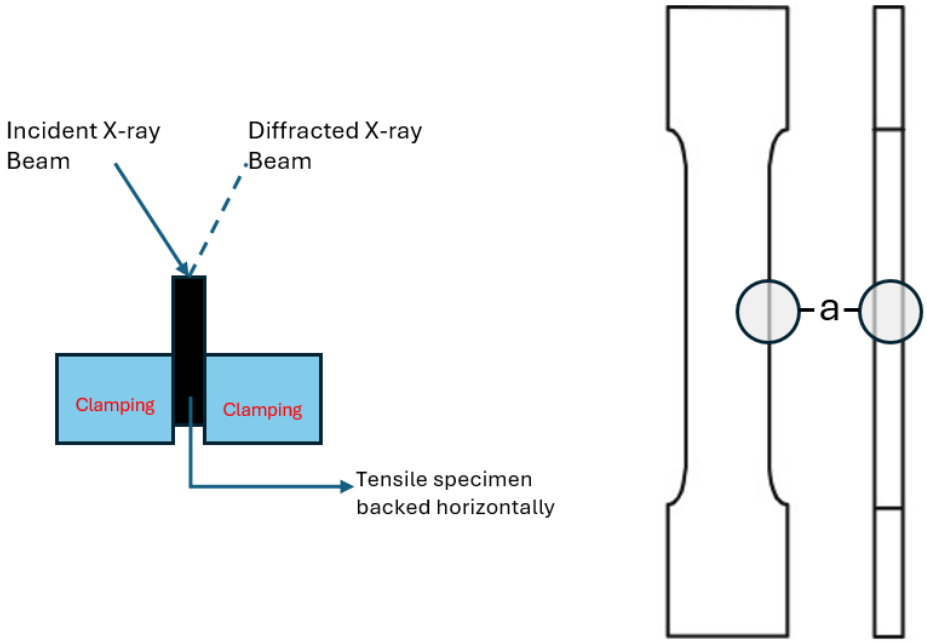

Fig. 4: Experimental setup for residual stress analysis. The left panel illustrates the clamping configuration, where multiple tensile specimens are stacked to form a stable block (black rectangle). The right panel details the measurement region, with (a) indicating the specific location of the X-ray diffraction (XRD) analysis.

The mathematical equation for XRD stress measurement connects surface stress to lattice strain, defined as the relative change in lattice spacing $(d_{\phi\psi} - d_0)/d_0$ [11]. Substituting this into stress-strain equations yields a fundamental linear relationship:

$$d_{\phi\psi} = \left[\left(\frac{1+\nu}{E} \right)_{(hkl)} \sigma_\phi d_0 \right] \sin^2 \psi + \text{Constant} \tag{2}$$

This equation reveals that lattice spacing $d_{\phi\psi}$ is a linear function of $\sin^2 \psi$. Consequently, the surface stress σ_ϕ can be calculated directly from the slope of the d versus $\sin^2 \psi$ plot [12]. In this

study, the residual stress of the four samples was calculated using the Xtronic software provided with the Machine Xstress G2R. The results are shown in the Figure 5.

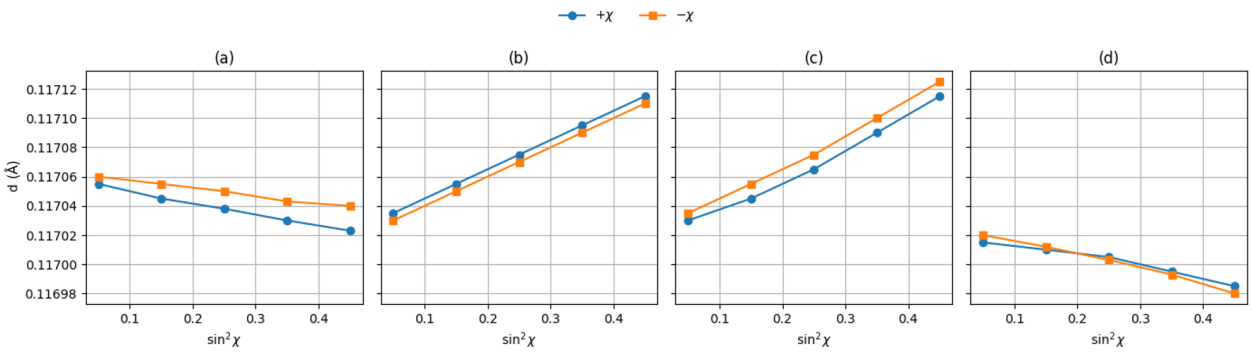

Fig. 5: Residual Stress results for the Four samples, a) Milled TS samples, b) Laser TS samples, c) EDM TS Samples, and finally d) Water Jet TS Samples

The phenomenon of elliptical curvature in d versus $\sin^2\psi$ plots, commonly referred to as "ψ-splitting," typically indicates the presence of shear stresses (σ_{13} and σ_{23}) acting normal to the surface or instrumental misalignment [13]. In the context of the plane-stress model assumed for these thin ferritic sheets, such shear components are expected to be negligible. The experimental results obtained in this study (Figure 5) exhibit a high degree of linearity with a slight separation between the positive and negative tilt data ($+\chi$ and $-\chi$) [14]. This absence of ψ-splitting confirms that shear stresses perpendicular to the surface have a low magnitude, thereby validating the instrument alignment and the application of the linear plane-stress model for the accurate calculation of residual stresses [13].

Table 2: Estimation of the residual stress for each cutting method

Type of Cutting methods	**EDM**	**Laser**	**Milling**	**Water Jet**
Estimate Residual Stress [MPa]	353.5±31.2	337.6±11.7	-90.5±5.0	-115.0±3.0
Type of Residual Stress	Tensile	Tensile	Compressive	Compressive

Residual stresses are calculated for each cutting method. Only the Laser and EDM cutting methods exhibit tensile residual stress, which results from the heat generated during the cutting process. In contrast, the Milling and Water Jet methods demonstrate compressive residual stress due to their mechanical cutting nature [15]. Therefore, Studies show that the residual stress can be adjusted by cooling the material during the process [16]. All results are presented in the Table. 2

Vickers hardness test.

To quantify localized hardening induced by the cutting process, Vickers hardness testing was performed on specimens extracted immediately after fabrication. Rectangular samples (15×12.5 mm) were prepared for the LECO LM100AT micro-hardness tester. The specimens were cold-mounted in epoxy resin, then ground and polished to a final surface finish of 3 μm. The testing procedure adhered to the DIN EN ISO 6507-1:2018 standard [17]. Utilizing a diamond indenter with a $136°$ apical angle [18], Multiple loads were tested to optimize measurement conditions. Based on this preliminary analysis, a test load of HV 0.025 was selected to ensure appropriate indentation size relative to the microstructural features.

During the procedure, the indenter is pressed into the specimen surface under a specific load. The hardness value (HV) is determined by the ratio of the maximum applied force (P) to the surface area

(A) of the resulting residual indentation as shown in the Equation 3. This area is calculated from the mean length of the indentation diagonals. A key advantage of this method is that the hardness value is independent of the load for homogeneous materials, making it a robust metric for assessing the resistance to plastic deformation.

$$HV \approx 1.854 \frac{P}{d^2} \tag{3}$$

The micro-hardness measurements were performed for all four cutting methods to quantify the depth of the process-induced hardening. The results, presented in Figure 6, demonstrate that while surface variations may exist, the hardness profiles for all samples converge to a uniform value at a depth of 0.24 mm. This convergence is significant for two reasons.

First, it confirms the consistency of the bulk material, verifying that the base properties of the ferritic steel sheets were identical across all samples and unaffected by either the cutting method or sample preparation.

Second, it establishes the localization of the cutting effect. Despite the low thermal capacity of the 0.25 mm thin sheets, the Heat Affected Zone (HAZ) for thermal processes and the plastic deformation zone for mechanical processes are restricted to the immediate edge. The return to nominal hardness at 0.240 mm proves that the cutting technologies do not alter the material's microstructure deep into the specimen, preserving the bulk mechanical integrity.

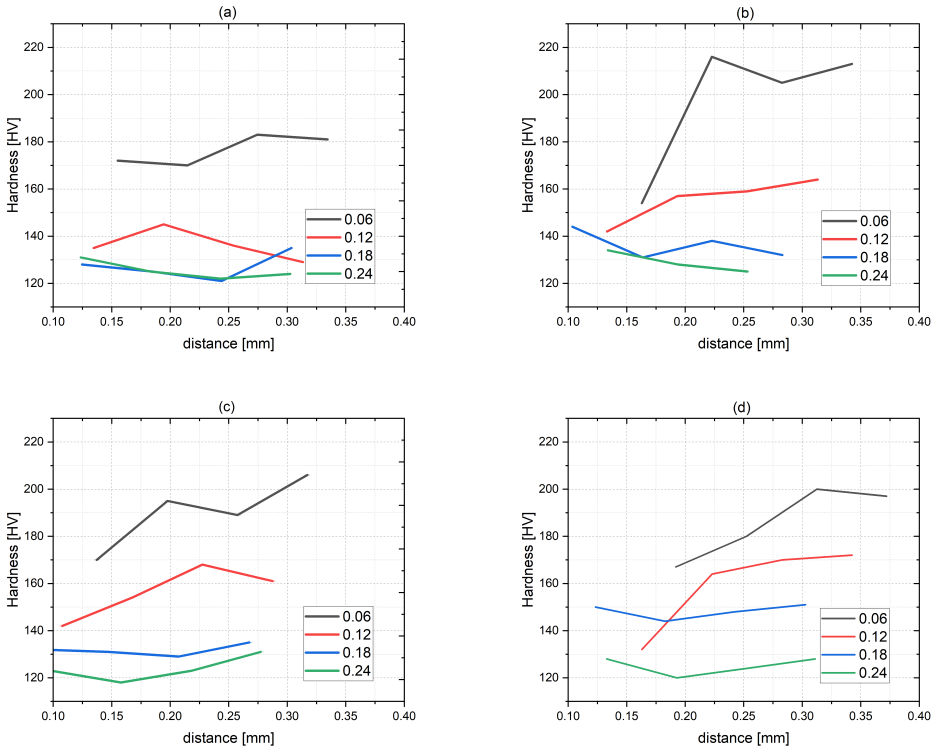

Fig. 6: Comparison of hardness profiles as a function of distance from the cut edge for different cutting processes at a different depth where : a) Milled TS samples, b) Laser TS samples, c) EDM TS Samples, and finally d) Water Jet TS Samples

Influence of cutting technology on the plastic region (Hollomon fit).

To evaluate the influence of the cutting process on the plastic behaviour of the thin ferritic sheets, the true stress-strain curves were analyzed using the hollomon power law relation in Equation 4 [19].

$$\sigma = K\epsilon^n \tag{4}$$

This analysis focuses on the work-hardening exponent (n) and the strength coefficient (K) to determine if the cutting thermal or mechanical energy altered the material's fundamental flow properties [20].

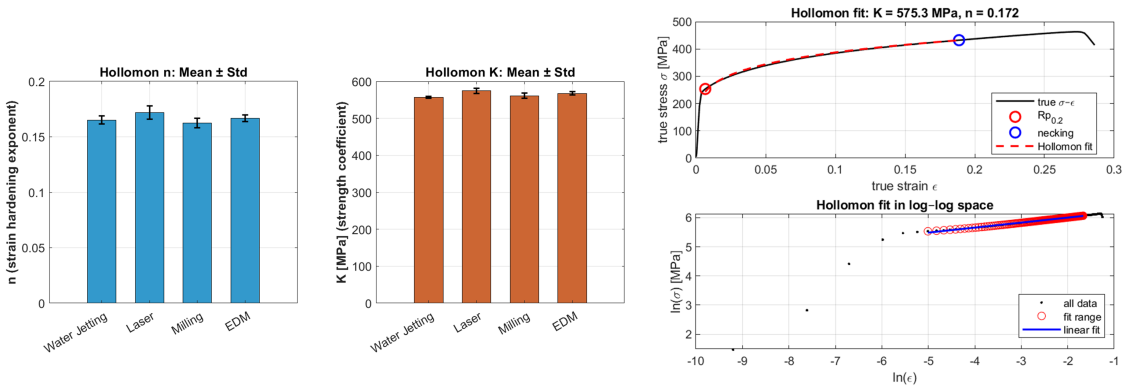

Fig. 7: Analysis of plastic flow behavior. (right) Representative True Stress-Strain curve and Hollomon fit (log-log) for the EDM-cut specimen. (left) Comparison of the strain hardening exponent (n) and strength coefficient (K) across all four cutting technologies. The error bars indicate standard deviation.

Figure 7 illustrates the consistency of the plastic behavior across all datasets, based on the six specimens tested for each cutting method. The results indicate high stability: the strain hardening exponent (n) settles within a narrow range of 0.175 ± 0.005, and the strength coefficient (K) remains constant at approximately 580 MPa. Notably, no statistically significant differences were observed among the cutting technologies.

This macroscopic consistency corroborates the micro-hardness findings presented in Figure 6. Although the cutting processes induce a localized HAZ or deformed layer, this region is confined to a depth of approximately 0.24 mm. Given the 12.5 mm width of the tensile specimen, this affected layer constitutes less than 4% of the total cross-sectional area. Consequently, the plastic flow response is dominated by the unaffected bulk material, confirming that while cutting-edge quality may influence the failure point (ductility), it does not impact the component's flow behavior (strength and hardening), Confirming that whatever cutting methods is chosen, the Flow curve for the development of a material card is not impacted [21].

Evolution of strain distribution and analysis of the failure region.

While the flow curves show similarity across all cutting methods, the local strain evolution reveals the critical role of edge quality in determining failure mechanisms. Digital Image Correlation (DIC) was employed to map the strain distribution at two distinct stages: ultimate tensile strength (UTS) and immediately prior to fracture.

To verify the repeatability of the results, DIC analysis was performed on three specimens per cutting method (selected from the six mechanically tested samples). Figure 8 presents the strain distribution at UTS for a representative specimen from each group.

The strain distribution maps reveal distinct localization behaviors that were consistent across the analyzed repetitions. For the Water Jet and Laser specimens, strain localization consistently concentrated along the cut edges in all samples, confirming that edge defects act as dominant crack initiation sites regardless of stochastic variations in failure location along the gauge length. In contrast, the Milled specimens repeatedly exhibited a double high-strain region prior to necking, suggesting a more distributed deformation process. Finally, the EDM samples exhibited a highly reproducible unicellular localization pattern, characterized by a single high-strain region that develops into a central neck. To quantify the strain localization, a transverse line was defined across the center of the specimen

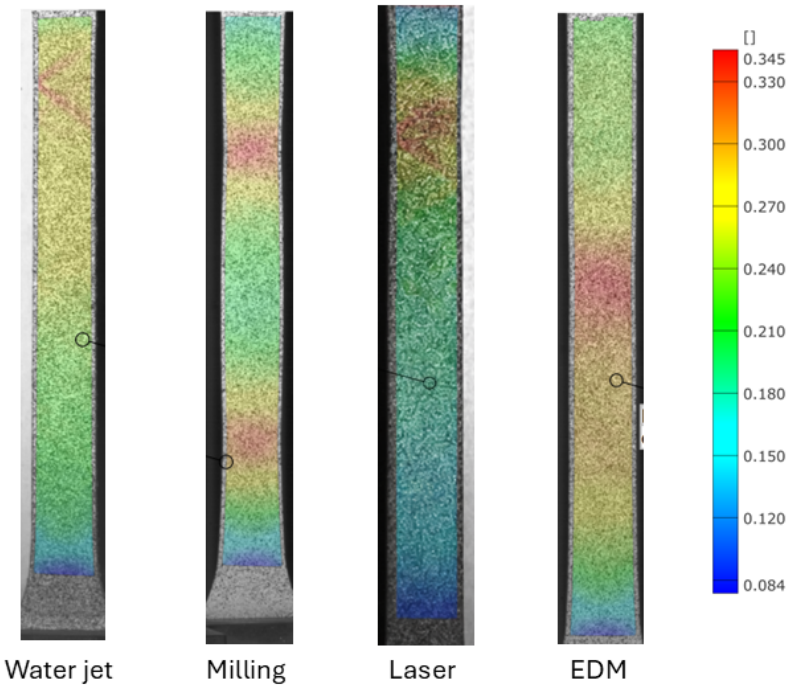

Fig. 8: DIC images of the tensile test at the UTS

gauge section. The strain distribution along this path was extracted at the Ultimate Tensile Strength (UTS) to evaluate specific differences in deformation behavior across the various cutting methods. The resulting profiles are presented in Figure 9.

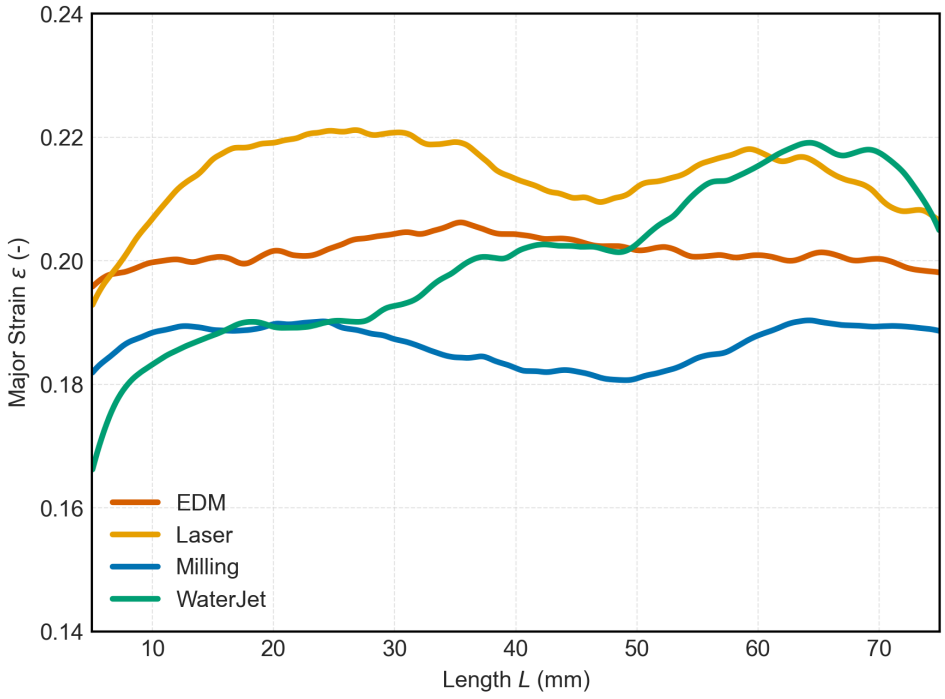

Fig. 9: Comparison of averaged major strain profiles extracted along the central constructed line across the tensile specimens at the Ultimate Tensile Strength (UTS)

To quantify the spatial evolution of deformation, strain profiles were extracted along a central transverse path across the specimen length at the Ultimate Tensile Strength (UTS). These profiles, presented in Figure 9, provide a quantitative correlation of the strain observed in the DIC maps in Figure 8.

The strain profile for the milled specimen (blue line) exhibits a distinct double-peak, with strain maxima located at normalized widths of approximately 0.15 and 0.85. This quantitative profile aligns perfectly with the ”double high-strain region” observed in the DIC imagery. Physically, this suggests that the compressive residual stresses and low roughness at the milled edges effectively suppress localized edge yielding. Consequently, the material is forced to accommodate strain across a wider internal zone, delaying the formation of a single dominant neck.

In contrast, the Laser (orange) and Water Jet (green) profiles display pronounced asymmetry and instability. The Laser profile reveals a dominant strain peak significantly shifted from the center (near 0.25), while the Water Jet profile shows a rising strain gradient towards the opposite edge (near 0.75). These off-center peaks confirm that the deformation is not governed by bulk plasticity but rather by edge defects. The high roughness of the Water Jet and HAZ-induced tensile stresses of the Laser act as local stress concentrators.

The EDM profile (red) presents a stable, plateau-like distribution across the central gauge width (0.2 to 0.8), with a single, slight central peak. This ”normal” distribution indicates that, despite the thermal nature of the process, the edge conditions in EDM are sufficiently uniform to allow the material to deform homogeneously before necking, consistent with the unicellular strain field observed in the DIC maps.

To give a statistical overview of the deformation, the distribution of major strain values across the entire gauge area was analyzed at two critical stages: the onset of Ultimate Tensile Strength (UTS) and immediately prior to Failure. The resulting boxplots are presented in Figure 10.

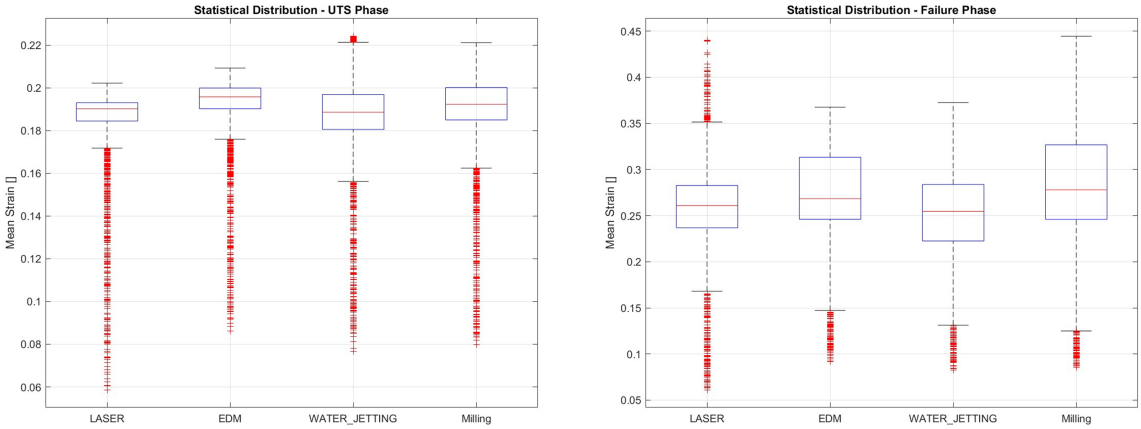

Fig. 10: Statistical distribution of major strain across the specimen gauge area at (left) the Ultimate Tensile Strength (UTS) and (right) the Failure phase. The red line indicates the median, the box represents the interquartile range (IQR)

The Uniform Elongation at the UTS region (Figure 10, left) reveals a high degree of similarity across all four cutting methods. The median strain values cluster tightly around 0.19, with comparable interquartile ranges (IQR). This statistical uniformity reinforces the Hollomon analysis (Figure 7), confirming that the bulk plastic behavior up to the point of instability is governed by the material’s intrinsic properties rather than the edge condition.

In contrast, the Failure phase (Figure 10, Right) shows some divergence. The milled samples exhibit the highest median strain (≈ 0.28) and the widest distribution. This correlates with the ”bimodal” strain profile observed earlier, confirming that the compressive residual stresses and low roughness

enable the material to accommodate significantly more plastic deformation during necking before fracture.

The EDM specimens have a transitional position with a median strain of ≈ 0.27. Despite being a thermal process with tensile residual stresses, the EDM edge is sufficiently uniform to avoid the premature strain localization observed in Laser cutting, resulting in normal failure behavior.

On the other hand, the Laser and water jet samples show slightly lower median strains (≈ 0.26). The tensile residual stresses (Laser) and high-roughness (Water Jet) act as failure accelerators.

Conclusion

This study presented a multi-analytical characterization of the impact of four distinct cutting technologies (Laser, EDM, Milling, and Water Jet) on the edge integrity and tensile performance of thin ferritic steel sheets. By integrating optical microscopy, roughness measurements, X-ray diffraction (XRD), and micro-hardness profiling with DIC-coupled tensile testing, we established a direct correlation between manufacturing-induced edge states and mechanical behavior.

The applicability of X-ray diffraction (XRD) to this type of specimen was evaluated, considering the geometric constraints imposed by the $0.25mm$ edge that prevent the use of standard comparative methods, such as hole-drilling. To ensure the reliability of the X-ray diffraction data, strict internal quality metrics were applied. The high linearity of the lattice spacing plots (d vs. $\sin^2\psi$) and the absence of ψ-splitting confirmed that the stress state at the cut edge adheres to the theoretical plane-stress model with negligible shear components. This effectively verifies the $\sin^2\psi$ method as a robust and necessary tool for non-destructive quality control of thin-gauge cut edges.

Micro-hardness depth profiles and Hollomon analysis of the plastic flow curves demonstrated that the process-induced material alteration is strictly localized. Hardness values converged to the base-material baseline at a depth of 0.24 mm, and strain-hardening exponents ($n \approx 0.18$) were consistent across all samples. This confirms that the bulk mechanical integrity of the thin sheet remains unaffected by the cutting method and that it also doesn't affect the flow curve, especially if the tests are used for making a material card for simulating a forming process.

Finally, while the bulk plastic flow remains uniform across all the cutting methods, the post-necking ductility is fundamentally governed by edge surface integrity. Milling proved superior, delivering the highest ductility and a characteristic bimodal strain distribution, as the combination of compressive residual stresses and low roughness effectively suppressed edge cracking. EDM exhibited high ductility and stable necking comparable to milling, a performance attributed to its uniform edge morphology despite the presence of tensile residual stresses. Therefore, the Laser and Water Jet cutting resulted in the lowest strain-to-failure, where severe tensile stresses and high surface roughness acted as stress concentrators, leading to a strain localization and significantly reducing the material's total deformation capacity, resulting in an edge crack.

References

[1] A Bond, J Marshall, and H Dundas. Resistance of ferritic stainless steels to stress corrosion cracking. In *Stress Corrosion Testing*, pages 116–126. ASTM International, 1967.

[2] Yong Hou, Dongjoon Myung, Jong Kyu Park, Junying Min, Hyung-Rim Lee, Ali Abd El-Aty, and Myoung-Gyu Lee. A review of characterization and modelling approaches for sheet metal forming of lightweight metallic materials. *Materials*, 16(2):836, 2023.

[3] NA Abukhshim, PT Mativenga, and M Aslam Sheikh. Heat generation and temperature prediction in metal cutting: A review and implications for high speed machining. *International Journal of Machine Tools and Manufacture*, 46(7-8):782–800, 2006.

[4] Kiha Lee and David A Dornfeld. Micro-burr formation and minimization through process control. *Precision Engineering*, 29(2):246–252, 2005.

[5] Metmac. The Future of Sheet Metal Cutting Machines: Trends and Innovations, August 2024. Accessed: 2026-01-19.

[6] International Organization for Standardization. Metallic materials – tensile testing – part 1: Method of test at room temperature, 2019.

[7] ME Hilly. Residual stress measurement by x-ray diffraction. *SAE Information Report*, 784, 1971.

[8] Ismail C Noyan and Jerome B Cohen. *Residual stress: measurement by diffraction and interpretation*. Springer, 2013.

[9] Stresstech. Xstress G2R: Portable Residual Stress and Retained Austenite Analyzer, November 2021. Presentation V2.2.

[10] Nicolae Burnete and Bogdan Ovidiu Varga. *Proceedings of the 4th International Congress of Automotive and Transport Engineering (AMMA 2018)*. Springer, 2018.

[11] Hui Liu, Daniel Schraknepper, and Thomas Bergs. Investigation of residual stresses and workpiece distortion during high-feed milling of slender stainless steel components. *Procedia CIRP*, 108:495–500, 2022.

[12] Yves Pauleau. Residual stresses in physically vapor-deposited thin films. In *Handbook of Thin Films*, pages 455–522. Elsevier, 2002.

[13] MOHAMMED BELASSEL, James A Pineault, and Michael E Brauss. Origin and interpretation of psi-splitting and out of plane shear stress when using diffraction techniques. 2025.

[14] Arijit Lodh, Khushahal Thool, and Indradev Samajdar. X-ray diffraction for the determination of residual stress of crystalline material: an overview. *Transactions of the Indian Institute of Metals*, 75(4):983–995, 2022.

[15] Alexander Leonard Meijer, Dominic Stangier, Wolfgang Tillmann, and Dirk Biermann. Induction of residual compressive stresses in the sub-surface by the adjustment of the micromilling process and the tool´s cutting edge. *CIRP Annals*, 71(1):97–100, 2022.

[16] Julius Schoop and IS Jawahir. Physics-based modelling and validation of dynamically varying thermal and mechanical residual stress fields in finish machining of aerospace alloys. *CIRP Annals*, 2025.

[17] DIN EN ISO 6507-1. Metallische werkstoffe – härteprüfung nach vickers – teil 1: Prüfverfahren (iso 6507-1:2018), 7 2018.

[18] AE Giannakopoulos, P-L Larsson, and R Vestergaard. Analysis of vickers indentation. *International journal of solids and structures*, 31(19):2679–2708, 1994.

[19] John H Hollomon. Tensile deformation. *Aime Trans*, 12(4):1–22, 1945.

[20] Matthew A Davies and Timothy J Burns. Thermomechanical oscillations in material flow during high-speed machining. *Philosophical Transactions of the Royal Society of London. Series A: Mathematical, Physical and Engineering Sciences*, 359(1781):821–846, 2001.

[21] Fabian Knieps, Manuel Köhl, and Marion Merklein. Local strain measurement in tensile test for an optimized characterization of packaging steel for finite element analysis. *Key Engineering Materials*, 883:309–316, 2021.